

Adaptive multilayer level set method for segmenting images with intensity inhomogeneity

Guopeng Huang¹, Hongbing Ji¹✉, Wenbo Zhang¹, Zhigang Zhu¹

¹School of Electronic Engineering, Xidian University, 2 South Taibai Road, Xi'an Shaanxi, 710071, People's Republic of China

✉ E-mail: hbji@xidian.edu.cn

Abstract: The level set method based on bias correction can segment images with gentle intensity inhomogeneity effectively. However, most level set methods fail to segment severe inhomogeneous images due to the use of fixed scale clustering criterion. To deal with this problem, an adaptive multilayer level set method is proposed to segment images with severe intensity inhomogeneity. First, an improved global adaptive scale operator and a local adaptive scale operator are designed to adaptively adjust the scale of clustering kernel function according to the degree of intensity inhomogeneity. Then, an adaptive multilayer level set structure is constructed with the two designed scale operators. The number of layers and the scale of each layer in the multilayer structure are adaptively determined based on the degree of intensity inhomogeneity, which not only provides appropriate candidate scales in each pixel but also allows the model to detect global contrast information. With the dual minimisation method, image segmentation and bias correction can be achieved simultaneously. In addition, a hybrid bias field initialisation procedure is proposed to enhance the robustness of the proposed method. Experimental results demonstrate the effectiveness and robustness of the proposed method in segmenting images with intensity inhomogeneity.

1 Introduction

Image segmentation plays a vital role in computer vision and image processing. The main challenges for image segmentation are noise, complex texture, and intensity inhomogeneity. In particular, it is difficult to segment images in the presence of intensity inhomogeneity due to the overlap of the intensity ranges between different object regions [1]. The active contour model (ACM) [2] has been widely applied in image segmentation because it can provide a smooth and closed contour to cover object boundary with sub-pixel precision. The level set method is a classic ACM, originally proposed by Osher and Sethian [3]. The level set method expresses contours as the zero-level set of a higher dimension function, usually called a level set function [1]. Since it can deal with complex topological changes [1], the level set method is widely used in image segmentation.

According to the image property embedded in the energy functional, the existing level set models can be categorised into two major classes: edge-based models [4–8] and region-based models [9–14]. Edge-based models mainly employ edge information for image segmentation [4]. However, these models are usually sensitive to noise and initial contour [9]. Region-based models utilise image statistical information to identify each region of interest. They are less sensitive to noise and initial contour and can deal with images with weak boundaries. One of the most popular region-based models is the Chan–Vese (CV) model [9], which is evolved from the well-known Mumford–Shah model [15]. Wu and He [11] proposed a strictly convex energy functional for two-phase image segmentation. However, most of the region-based models are based on the assumption of intensity homogeneity. Thus they are not applicable to images with intensity inhomogeneity. Subsequently, some local region-based models [16–23] have been proposed, which are based on the assumption that the image intensity in the local region is approximately homogeneous. Li *et al.* proposed the local binary fitting (LBF) model [16, 17]. Zhang *et al.* proposed the local image fitting model [19]. However, local region-based models are also sensitive to initial contour.

Intensity inhomogeneity is a common phenomenon in real-world images, which is usually caused by the defect of the imaging device or illumination variation. The inhomogeneous image is usually described as a true piecewise constant image multiplied by

a smooth and spatially varying field [24]. This field is referred to as the bias field. Some bias correction-based methods for image segmentation have been proposed [1, 25–31]. Li *et al.* proposed a multiplicative intrinsic component optimisation (MICO) model [25], which utilised a set of smooth basis functions to estimate the bias field. Feng *et al.* proposed a local inhomogeneous intensity clustering (LINC) model [26], which introduces the MICO model into the level set framework. The models based on *K*-means clustering have been widely concerned in recent years [1, 27–31]. These methods also assume that the image intensity in the local region is approximately homogeneous. They utilise the scale parameter of the clustering kernel function to control the size of each local region. Li *et al.* proposed the local intensity clustering (LIC) [1] model, which exploits a locally weighted *K*-means clustering method for image segmentation and bias correction. Zhang *et al.* proposed a locally statistical ACM (LSACM) [28], which introduces the global clustering variance information. Wang *et al.* [31] utilised two different local fitted images to construct a hybrid region intensity fitting (HRIF) energy functional. However, most of them are unable to cope with severe inhomogeneous images because of the use of fixed scale clustering criterion. Besides, these models are also sensitive to initial contour and are prone to fall into some local minima.

Generally, the scale parameter for the clustering kernel function should be selected appropriately according to the degree of intensity inhomogeneity [1]. Recently, some adaptive scale models [32–34] and multiscale methods [35–37] are proposed to segment images with intensity inhomogeneity. Cai *et al.* propose an adaptive scale ACM (ASACM) [33] based on image entropy and semi-naïve Bayesian classifier. A fast level set method for inhomogeneous image segmentation with adaptive scale parameter (FLSAS) is presented in [34]. However, the same scale in each pixel of these adaptive scale models may result in erroneous segmentation of images with non-linear and complicated intensity inhomogeneity. Wang *et al.* [36] employed multiscale low-pass filter (MSF) to estimate the bias field. Min *et al.* [37] proposed a novel dual minimisation (DM) model to segment images with intensity inhomogeneity. These multiscale models are capable of detecting global contrast information so as to avoid the model being trapped in local minima [37]. However, these methods with the fixed scale parameters provide limited scale candidates, which

may result in failure to provide appropriate scale parameters to segment the images with severe intensity inhomogeneity.

In this paper, an adaptive multilayer level set (AMLLS) method is proposed to segment images with severe intensity inhomogeneity. First, the degree of the local intensity inhomogeneity is measured by the local variance in the smooth regions. An improved global adaptive scale operator and a local adaptive scale operator are designed to adaptively adjust the scale of clustering kernel function according to the degree of local intensity inhomogeneity. Then, an AMLLS structure is constructed with the two designed scale operators. The number of layers and the scale of each layer in the multilayer structure are adaptively determined based on the degree of intensity inhomogeneity, which not only provides appropriate candidate scales in each pixel but also allows the model to detect global contrast information. With the DM method [37], image segmentation and bias correction can be achieved simultaneously, which can adaptively determine the optimal scale in each pixel. In addition, a hybrid bias field initialisation procedure is proposed based on the coefficient of joint variation (CJV) [24] to enhance the robustness of the proposed method.

The remainder of this paper is organised as follows. In Section 2, the related LIC model and DM model are briefly reviewed. Then the proposed method is described in Section 3. Section 4 presents the experimental results. Finally, the conclusion of this paper is presented in Section 5.

2 Background models

2.1 LIC model

Based on a commonly used image model, the LIC model [1] is proposed to segment images with intensity inhomogeneity. The inhomogeneous image model is defined as

$$I = bJ + n_0 \quad (1)$$

where I is the observed image, b is the bias field, J is the true image, and n_0 is the additive noise. The assumptions for the true image J and bias field b are as follows:

(A) b varies slowly over the entire image domain Ω .

(B) $J(x) \simeq c_i$ for $x \in \Omega_i$, where $\{\Omega_i\}_{i=1}^N$ is a partition of the image domain Ω .

The energy functional is defined as

$$E = \int \left(\sum_{i=1}^N \int_{\Omega_i} K_\sigma(y-x) |I(x) - b(y)c_i|^2 dx \right) dy \quad (2)$$

where $K_\sigma(x)$ is a kernel function, which is defined as

$$K_\sigma(u) = \begin{cases} e^{-u^2/2\sigma^2}/a, & |u| \leq 2\sigma \\ 0, & \text{else} \end{cases} \quad (3)$$

where a is the normalisation constant such that $\int K(u) = 1$, σ is the standard deviation (or the scale parameter).

The LIC model utilises a weighted K-means clustering method to estimate the bias field. With bias correction, the method can segment some images with intensity inhomogeneity. However, it is usually ineffective for some images with severe intensity inhomogeneity because of the use of fixed scale clustering criterion. Meanwhile, this model is also sensitive to initial contour.

2.2 DM model

The DM model [37] utilised a series of Gaussian kernel functions with different scales to construct a multilayer structure. The energy term E_M of the multilayer structure is

$$E_M = \{E_M^{(1)}, E_M^{(2)}, \dots, E_M^{(i)}, \dots\}, \quad i = 1, 2, \dots, m \quad (4)$$

$$\begin{aligned} E_M^{(i)} = \lambda_1 \iint K_{\sigma_i}(y-x) (I(x) - b^{(i)}(y) c_1^{(i)})^2 M_1(\phi(x)) dy dx \\ + \lambda_2 \iint K_{\sigma_i}(y-x) (I(x) - b^{(i)}(y) c_2^{(i)})^2 M_2(\phi(x)) dy dx \end{aligned} \quad (5)$$

where $E_M^{(i)}$, $b^{(i)}$, $c_1^{(i)}$, and $c_2^{(i)}$ denote energy term, bias field, intensity constants inside and outside the contour for the i th layer, respectively. $M_1(\phi) = H(\phi)$ and $M_2(\phi) = 1 - H(\phi)$ are the membership functions of each cluster. $K_{\sigma_i}(\cdot)$ is

$$K_{\sigma_i}(u) = \begin{cases} e^{-u^2/2\sigma_i^2}/a, & |u| \leq \sigma_i \\ 0, & \text{else} \end{cases}, \quad i = 1, 2, \dots, m \quad (6)$$

where $\sigma_i = \Delta s \cdot i + 1$ is the scale of the Gaussian kernel function, Δs is the scale interval between adjacent layers and m is the number of layers for the multilayer structure.

The final energy functional is defined as follows

$$\begin{aligned} E = \lambda_1 \int_{\Omega} \min_{i \in \{1, 2, \dots, m\}} (I(x) - b^{(i)}(x) c_1^{(i)})^2 M_1(\phi(x)) dx \\ + \lambda_2 \int_{\Omega} \min_{i \in \{1, 2, \dots, m\}} (I(x) - b^{(i)}(x) c_2^{(i)})^2 M_2(\phi(x)) dx \end{aligned} \quad (7)$$

The DM model can prevent the model from falling into local minima and adaptively determine the optimised evolution layer at each pixel to handle inhomogeneous images [37]. However, the fixed scale parameters of the multilayer structure in the DM model may lead to erroneous segmentation for images with severe intensity inhomogeneity.

3 Proposed method

3.1 Adaptive scale operators

In this section, the local variance is employed to measure the local image inhomogeneity and two new adaptive scale operators are proposed for the clustering kernel function.

3.1.1 Global adaptive scale operator: According to the inhomogeneous image model in (1) and assumptions (A) and (B) in the LIC model, the local intensity variations are caused by inhomogeneity in the smooth regions away from the real object boundary, ignoring the additive noise. Generally, the bias field is thought to be slowly varying. Thus, the local intensity variations are large in the regions near the object boundary, while small in the smooth regions. Therefore, the local variance in the smooth regions can be utilised to measure the degree of local image inhomogeneity. A global adaptive scale parameter method is proposed in [34]. However, the obtained smooth region is susceptible to noise. Therefore, the method of obtaining smooth regions is simplified and an improved global adaptive scale operator is proposed in this section.

To mitigate the effects of noise, the observed image I is pre-processed using a median filter and a bilateral filter to obtain I_1 . Then, the Laplacian operator of Gaussian is utilised to detect the target boundary C_L roughly. The local regions near the object boundary may contain both object and background pixels. Therefore, the regions near the estimated boundary C_L is removed, and the final smooth regions Ω_s is

$$\Omega_s = \{x | \text{dist}(x, C_L) > w_0 + 1\}, \quad x \in \Omega \quad (8)$$

where w_0 is a constant parameter, $\text{dist}(x, C_L)$ is the Euclidean distance between x and the closest pixel on C_L .

After obtaining the smooth region Ω_s , the local variance $D(x)$ in a $(2w_0 + 1) \times (2w_0 + 1)$ square neighbourhood region $R^{w_0}(x)$ in the smooth region Ω_s of image I_1 can be obtained. Since the bias field is thought as slowly varying [1], the mean of the local variance in smooth regions is utilised to measure the degree of global intensity

inhomogeneity. Generally, the scale parameter is inversely proportional to the degree of image inhomogeneity. Therefore, an improved global adaptive scale operator σ_G is designed for kernel function

$$\sigma_G = \alpha / (\sqrt{c_D})^p \quad (9)$$

where α and p are constant parameters, c_D is the mean of $D(x)$ in Ω_s for the image I_1 .

This global adaptive scale operator provides small scale parameters for images with severe intensity inhomogeneity and large scale parameters for images with slight intensity inhomogeneity. Therefore, the global adaptive scale operator can make the K -means clustering-based methods robust to intensity inhomogeneity.

3.1.2 Local adaptive scale operator: The presented global adaptive scale parameter provides an appropriate and uniform scale for all pixels. However, it may be ineffective for images with nonlinear and complicated intensity inhomogeneity. The scale parameter in each pixel should be adaptively adjusted according to the degree of the local intensity inhomogeneity. The local variance $D(x)$ is utilised to measure the degree of the local intensity inhomogeneity at each pixel. Since the bias field varies slowly over the image domain [1], a local adaptive scale operator σ_L for each pixel is proposed

$$\sigma_L(x) = \begin{cases} 0.5\sigma_G, & x \notin \Omega_s \& D(x) > 4c_D \\ \sigma_G - \frac{2\sigma_G}{\pi} \arctan\left(\frac{\sqrt{D(x)} - \sqrt{c_D}}{\varsigma + \sqrt{c_D}}\right), & \text{else} \end{cases} \quad (10)$$

where ς is a constant parameter.

The local adaptive scale operator adaptively provides appropriate scale parameter between the values of zero and twice the global adaptive scale parameters for each pixel, which prevents the scale from being too large or too small. The larger the local variance of the pixel, the smaller the scale parameter, and vice versa. Meanwhile, the local variance in the estimated boundary regions is very large. The regions near the object boundary usually have homogeneous intensity distributions, and too small scale parameters may make the level set converge slowly. Therefore, the minimum value of the scale parameter is limited to half of σ_G in the estimated boundary regions. Therefore, the local adaptive scale operator can provide an appropriate scale parameter for each pixel according to the degree of the local intensity inhomogeneity.

3.2 Adaptive multilayer structure

With the assumption of local intensity homogeneity, the K -means clustering-based methods are essentially based on the local region information to segment images. Therefore, they are not able to detect global contrast information and are prone to fall into local minima. The multiscale structure is capable of detecting global contrast information, but cannot handle images with severe intensity inhomogeneity due to the use of fixed scale parameters. Therefore, the two proposed adaptive scale operators are utilised to construct an AMLLS structure.

The scale parameters of the clustering kernel function play a vital role in the multilayer structure. Layers with smaller scales contain more local intensity distribution details, while the layers with large scales contain more global information. The local adaptive scale operator can be utilised to measure the degree of the local intensity inhomogeneity at each pixel. Therefore, the local adaptive scale parameter is employed to construct the first layer of the multilayer structure to better fit the image intensity. The scale

parameters for the first layer of the adaptive multilayer structure is defined as

$$\sigma_{ML}^{(1)}(x) = \beta \cdot \sigma_L(x) + 1 \quad (11)$$

where β is a constant parameter.

Since it can measure the degree of global intensity inhomogeneity, the global adaptive scale operator is utilised to adaptively determine the scale parameters of the other layers in the adaptive multilayer structure. The scale parameters for the i th ($i > 1$) layer of the adaptive multilayer structure is defined as

$$\sigma_{ML}^{(i)}(x) = \Delta s \cdot i + 1 = \beta \cdot \sigma_G \cdot i + 1 \quad (12)$$

The scale interval $\Delta s = \beta \cdot \sigma_G$ between adjacent layers in (12) adaptively varies with the degree of the image global intensity inhomogeneity. Equation (12) provides small Δs for images with severe intensity inhomogeneity and large Δs for images with slight intensity inhomogeneity. Meanwhile, the largest scale of the multilayer structure should be large enough to cover the image to detect global contrast information. Thus, the number of layers m is determined by Δs and the image size

$$m = \text{round}\left(\min\left(\left(\frac{N_0}{\pi}\right)^{0.5} / (4 \cdot \Delta s), \frac{T}{\Delta s}\right)\right) + 1 \quad (13)$$

where T is a constant parameter, which is used to constrain the maximum scale. N_0 is the number of pixels in the image. For images with severe intensity inhomogeneity, large m can provide more candidate scales to deal with the image. For images with slight intensity inhomogeneity, the method can converge quickly with small m .

The scale parameters for the i th layer of the adaptive multilayer structure is

$$\sigma_{ML}^{(i)}(x) = \begin{cases} \beta \cdot \sigma_L(x) + 1, & i = 1 \\ \beta \cdot \sigma_G \cdot i + 1, & i = 2, 3, \dots, m \end{cases} \quad (14)$$

With the scale parameters in (14) for the Gaussian kernel functions, the E_M of the multilayer structure is

$$E_M = \{E_M^{(1)}, E_M^{(2)}, \dots, E_M^{(i)}, \dots\}, \quad i = 1, 2, \dots, m \quad (15)$$

$$E_M^{(i)} = \sum_{j=1}^N \lambda_j \iint K_{\sigma_{ML}^{(i)}} \cdot (I(x) - b^{(i)}(y)c_j^{(i)})^2 M_j(\phi(x)) dy dx \quad (16)$$

Since each pixel is assigned a different scale parameter in the first layer, it is very complicated to implement $E_M^{(1)}$. The scale parameters in the first layer will be discretised to simplify the operation. The discrete scale parameters with equal interval τ can be expressed as

$$\sigma_D^{(j_0)} = \min(\sigma_{ML}^{(1)}) + (j_0 - 0.5) \cdot \tau, \quad j_0 = 1, 2, \dots, m_1 \quad (17)$$

where $\tau = (\max(\sigma_{ML}^{(1)}) - \min(\sigma_{ML}^{(1)}))/m_1$, m_1 is a constant parameter. With the discrete scale parameters, $E_M^{(1)}$ can be obtained by

$$E_M^{(1)} = \sum_{j=1}^N \lambda_j \int e_j(x) M_j(\phi(x)) dx \quad (18)$$

where $\delta_0(x)$ equals 1 if $x = 0$, and 0 otherwise. $e_j(x) = \sum_{j_0=1}^{m_1} \int \delta_0(L_{\sigma_D}(y) - j_0) K_{\sigma_D^{(j_0)}}(y - x) (I(x) - b^{(1)}(y)c_j^{(1)})^2 dy$ and $L_{\sigma_D} = \lceil (\sigma_{ML}^{(1)} - \min(\sigma_{ML}^{(1)}))/\tau \rceil$.

3.3 Level set formulation and numerical computation

In each pixel, the adaptive multilayer structure utilises local region information with different scales to estimate the clustering centre. With the DM method [37], the optimal evolution layer, at which the estimated clustering centre best fits the image intensity, is used to construct the level set energy functional. Image segmentation and bias correction can be achieved simultaneously by minimising the energy functional.

3.3.1 Energy functional: The multilayer intensity difference between the estimated clustering centre and the image intensity for the i th layer of the adaptive multilayer structure in each pixel is defined as

$$DI_j^{(i)}(x) = \begin{cases} e_j(x), & i = 1 \\ (I(x) - b^{(i)}(x)c_j^{(i)})^2, & i = 2, \dots, m \end{cases} \quad (19)$$

The optimal evolution layer is determined by minimising the multilayer intensity difference in each pixel. In general, the regions near the object boundary usually have homogeneous intensity distributions. Therefore, small scales in the regions near the object boundary enable the model to accurately extract the target boundary. Thus, the first layer is set as the optimal evolution layer in the regions near the object boundary. The optimal evolution layer $L_j(x)$ for the adaptive multilayer structure is

$$L_j(x) = \begin{cases} 1, & x \notin \Omega_s \\ \arg \min_i (DI_j^{(i)}(x)), & x \in \Omega_s \end{cases}, \quad j = 1, \dots, N \quad (20)$$

With the optimal layer $L_j(x)$ in (20), the optimal intensity difference $z_j(x)$ can be obtained by

$$z_j(x) = DI_j^{(L_j(x))}(x), \quad j = 1, \dots, N \quad (21)$$

The level set energy functional is defined with the intensity differences of the optimal evolution layer as follows

$$E_D = \sum_{j=1}^N \lambda_j \int_{\Omega} z_j(x) \cdot M_j(\phi(x)) dx \quad (22)$$

In addition, the level set function should be regularised to maintain the stability of the level set evolution [5, 17, 38]. In this paper, the widely used length item and regularisation item proposed in [17] are introduced to the proposed method. For the case of $N = 2$, the final level set energy functional is defined as follows

$$\begin{aligned} E = & \lambda_1 \int_{\Omega} z_1(x) H(\phi(x)) dx + \lambda_2 \int_{\Omega} z_2(x) (1 - H(\phi(x))) dx \\ & + \mu \cdot \int_{\Omega} |\nabla H(\phi)| dx + \nu \cdot \int_{\Omega} \frac{1}{2} (|\nabla \phi| - 1)^2 dx \end{aligned} \quad (23)$$

The two-phase formulation is also extended to a multi-phase one. k -level set function $\phi_1, \phi_2, \dots, \phi_k$ is utilised to represent the region $\Omega_i, i = 1, 2, \dots, N$. The corresponding membership function M_i of the region Ω_i is written as

$$M_i(\Phi(x)) = M_i(\phi_1(x), \phi_2(x), \dots, \phi_k(x)) = \begin{cases} 1, & x \in \Omega_i \\ 0, & \text{else} \end{cases} \quad (24)$$

where $\Phi = (\phi_1, \phi_2, \dots, \phi_k)$. In the case of $N = 3$, two-level set functions ϕ_1 and ϕ_2 are used to define the partitions of the image domain Ω , and the membership functions are $M_1(\Phi) = H(\phi_1)H(\phi_2)$, $M_2(\Phi) = H(\phi_1)(1 - H(\phi_2))$, and $M_3(\Phi) = 1 - H(\phi_1)$. The multi-phase energy functional is

$$\begin{aligned} E = & \sum_{j=1}^N \lambda_j \int_{\Omega} z_j(x) \cdot M_j(\Phi(x)) dx \\ & + \mu \cdot \sum_{q=1}^k \int_{\Omega} |\nabla H(\phi_q)| dx + \nu \cdot \sum_{q=1}^k \int_{\Omega} \frac{1}{2} (|\nabla \phi_q| - 1)^2 dx \end{aligned} \quad (25)$$

3.3.2 Energy minimisation: Minimising E in (23) or (25) with respect to each of its variables, their closed-form solutions can be obtained. For fixed ϕ and $b^{(i)}$, the optimal $c_j^{(i)}$ can be obtained by minimising $E_M^{(i)}$ in (15)

$$c_j^{(i)} = \frac{\int \sum_{j_0=1}^{m_1} ((b^{(1)*} K_{\sigma_D^{(j_0)}}) \delta_0(L_{\sigma_D}(x) - j_0)) IM_j(\phi) dx}{\int \sum_{j_0=1}^{m_1} ((b^{(1)} \cdot K_{\sigma_D^{(j_0)}})^2) \delta_0(L_{\sigma_D}(x) - j_0) M_j(\phi) dx} \quad (26)$$

$$c_j^{(i)} = \frac{\int (b^{(i)*} K_{\sigma_{ML}^{(i)}}) \cdot I \cdot M_j(\phi) dx}{\int ((b^{(i)})^2 K_{\sigma_{ML}^{(i)}}) \cdot M_j(\phi) dx}, \quad i = 2, \dots, m \quad (27)$$

where the sign $*$ is the convolution operation, the kernel function in (6) is utilised in the proposed method.

For fixed ϕ and $c_j^{(i)}$, the optimal $b^{(i)}$ can be obtained by minimising $E_M^{(i)}$ in (15)

$$b^{(1)} = \frac{\sum_{j_0=1}^{m_1} \left(\left(\sum_{j=1}^N c_j^{(1)} M_j(\phi) I \right) * K_{\sigma_D^{(j_0)}} \right) \delta_0(L_{\sigma_D}(x) - j_0)}{\sum_{j_0=1}^{m_1} \left(\left(\sum_{i=1}^N (c_j^{(1)})^2 M_j(\phi) \right) * K_{\sigma_D^{(j_0)}} \right) \delta_0(L_{\sigma_D}(x) - j_0)} \quad (28)$$

$$b^{(i)} = \frac{\left(I \cdot \left(\sum_{j=1}^N c_j^{(i)} M_j(\phi) \right) \right) * K_{\sigma_{ML}^{(i)}}}{\left(\sum_{j=1}^N (c_j^{(i)})^2 M_j(\phi) \right) * K_{\sigma_{ML}^{(i)}}}, \quad i = 2, \dots, m \quad (29)$$

In the case of $N = 2$, the minimisation of E in (23) with respect to ϕ can be achieved by solving the following gradient flow equations with fixed $b^{(i)}$, $c_j^{(i)}$, and L_j

$$\begin{aligned} \frac{\partial \phi}{\partial t} = & - \frac{\partial E}{\partial \phi} = - \delta(\phi)(\lambda_1 z_1 - \lambda_2 z_2) + \mu \delta(\phi) \operatorname{div} \left(\frac{\nabla \phi}{|\nabla \phi|} \right) \\ & + \nu \left(\nabla^2 \phi - \operatorname{div} \left(\frac{\nabla \phi}{|\nabla \phi|} \right) \right) \end{aligned} \quad (30)$$

where $\delta(\cdot)$ is the Dirac function, ∇ is the gradient operator, and $\operatorname{div}(\cdot)$ is the divergence operator.

The bias field for every layer can be estimated for the adaptive multilayer structure. The optimal evolution layer L_j in (20) can provide the optimal local information to fit the image in the segmentation regions Ω_j . Therefore, the bias field of the image can be defined as

$$b(x) = \begin{cases} b^{(L_1(x))}(x), & \phi(x) > 0 \\ b^{(L_2(x))}(x), & \phi(x) \leq 0 \end{cases} \quad (31)$$

In the case of $N \geq 3$, the minimisation of E in (25) with respect to the variable $\Phi = (\phi_1, \phi_2, \dots, \phi_k)$ can be achieved by solving the following gradient flow equations with fixed $b^{(i)}$, $c_j^{(i)}$, and L_j

$$\begin{aligned} \frac{\partial \phi_q}{\partial t} = & - \frac{\partial E}{\partial \phi_q} = - \sum_{j=1}^N \lambda_j z_j \frac{\partial M_j(\Phi)}{\partial \phi_q} + \mu \delta(\phi_q) \operatorname{div} \left(\frac{\nabla \phi_q}{|\nabla \phi_q|} \right) \\ & + \nu \left(\nabla^2 \phi_q - \operatorname{div} \left(\frac{\nabla \phi_q}{|\nabla \phi_q|} \right) \right), \quad q = 1, \dots, k \end{aligned} \quad (32)$$

3.3.3 Hybrid bias field initialisation: The segmentation is achieved by the evolution of the level set energy functional, which is an interactive iterative process. Before each iteration, the estimated bias fields $b^{(i)}$ in the previous iteration usually are used to initialise the bias fields of the multilayer structure, which allows

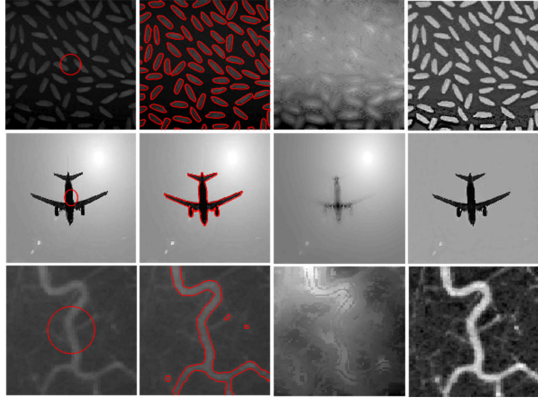


Fig. 1 Segmentation results by the proposed method on three images with intensity inhomogeneity. From the first to last column: the original images with initial contours, the segmentation results, the estimated bias fields, and the bias-corrected images

the algorithm to converge smoothly. However, the estimated bias fields also make the algorithm easy to fall into local minima. Meanwhile, the DM method [37] utilised a simple bias field initialisation procedure, $b_0^{(i)}(x) = 1$ for $x \in \Omega$, which allows the DM model to segment some images accurately and efficiently. However, the simple bias field initialisation procedure will make the segmentation unstable and incorrect for images with a large overlap of the intensity ranges between interior and exterior object regions. To make the algorithm more robust, the CJV [24], which can estimate the overlap between two different objects, is utilised to construct a hybrid bias field to initialise the bias field before each iteration. For the n th iteration, the hybrid bias field hb_n for the i th layer of the multilayer structure is

$$hb_n^{(i)}(x) = (1 - \omega_n)b_0^{(i)}(x) + \omega_n b_{n-1}^{(i)}(x), \quad i = 1, 2, \dots, m \quad (33)$$

where $b_0^{(i)}(x) = 1$ is the initial bias field, $b_{n-1}^{(i)}(x)$ is the estimated bias field after $n - 1$ iterations for the i th layer of the multilayer structure. The weight ω_n is designed as

$$\omega_n = 1 - e^{-\text{CJV}(\phi^{n-1})^2/4} \quad (34)$$

where ϕ^{n-1} is the level set function after $n - 1$ iterations. The CJV is defined as

$$\text{CJV}(\phi) = \frac{\sigma(\Omega_1) + \sigma(\Omega_2)}{|c(\Omega_1) - c(\Omega_2)|} \quad (35)$$

where $\Omega_1 = \{x \in \Omega | \phi(x) < 0\}$, $\Omega_2 = \{x \in \Omega | \phi(x) \geq 0\}$. $c(\cdot)$ and $\sigma(\cdot)$ are the image intensity mean and standard deviation in the region, respectively.

3.3.4 Numerical implementation: The explicit finite difference scheme is utilised to discretise (30) as follows

$$\frac{\phi^n - \phi^{n-1}}{\Delta t} = \frac{\partial \phi^n}{\partial t} \quad (36)$$

where Δt is the time-step and n denotes the iteration number. The Heaviside function $H(\phi)$ is regularised by

$$H_\epsilon(\phi) = \frac{1}{2} \left[1 + \frac{2}{\pi} \cdot \arctan \left(\frac{\phi}{\epsilon} \right) \right] \quad (37)$$

where ϵ is a constant parameter. $\delta(\phi)$ is approximated by

$$\delta_\epsilon(\phi) = H'_\epsilon(\phi) = \frac{1}{\pi} \frac{\epsilon}{\epsilon^2 + \phi^2} \quad (38)$$

The main process of the proposed AMLLS method for two-phase segmentation is summarised as follows:

Step 1: Compute σ_G , σ_L by (9) and (10).

Step 2: Construct $\sigma_{ML}^{(i)}$ by (14).

Step 3: Initialise $b_0^{(i)} = 1$, $n = 1$, and $\phi^0(x) = \begin{cases} -1, & x \in \Omega_0 \\ 1, & \text{else} \end{cases}$, where Ω_0 is a subset of Ω .

Step 4: Compute $hb_n^{(i)}$ by (33) and initialise the bias field $b^{(i)}$.

Step 5: Compute $c_j^{(i)}$ by (26) to (27).

Step 6: Compute $b^{(i)}$ by (28) to (29).

Step 7: Compute L_j according to (20) and compute z_j by (21).

Step 8: Evolve the level set function ϕ according to (30) and (36). Step 9: The algorithm ends if the maximum iteration number is reached or the level set function has converged, or else $n = n + 1$ and return to Step 4.

4 Experimental results

In this section, the performance of the proposed AMLLS method is evaluated. All of the experiments are conducted in the MATLAB R2017a (64bit) programming environment on a personal computer with an Intel Core i3 Duo 3.90 GHz CPU, 8 GB RAM, and Windows7 (64bit) operating system. In the experiments, unless otherwise specified, the default parameters are set as $w_0 = 1$, $\alpha = 5.2$, $\beta = 0.95$, $p = 1.25$, $\varsigma = 1$, $m_1 = 6$, $T = 32$, $\Delta t = 0.1$, $\epsilon = 1.5$, $\lambda_1 = \lambda_2 = 1$, $\nu = 1$ and $\mu = 0.0001 \times 255^2$.

The Jaccard similarity (JS) [24] is used to compare the segmentation performances of the models quantitatively. The metric is defined as

$$JS = \frac{N(S_g \cap S_m)}{N(S_g \cup S_m)} \quad (39)$$

where $N(\cdot)$ represents the number of pixels in the region. S_g indicates the foreground of the ground truth image and S_m stands for the foreground obtained by models. The closer the JS value is to one, the better the segmentation results are.

The performance of the proposed method is demonstrated in the case of two-phase segmentation first, followed by the multi-phase segmentation. The proposed AMLLS method is also compared with the LBF [17], LIC [1], MSF [36], LICD [30], LSACM [28], DM [37], LINC [26], HRIF [31], ASACM [33], and FLSAS [34] models on synthetic images, natural images, infrared images, and medical images with intensity inhomogeneity.

Fig. 1 shows the segmentation results of the proposed method on two nature images and one medical image. μ is set to 0.001×255^2 . The intensity inhomogeneity is obvious in these images. The proposed method can provide satisfactory segmentation results and estimate the bias field simultaneously. The image intensities within the regions inside and outside the contour become quite homogeneous in the bias-corrected images. Therefore, the proposed method has satisfactory performance in inhomogeneous image segmentation and bias field estimation.

Fig. 2 shows the segmentation results of the proposed method on one synthetic image, one infrared image and two medical images with severe intensity inhomogeneity. μ is set to 0.001×255^2 , 0.0026×255^2 , 0.02×255^2 , and 0.001×255^2 for the images, respectively. The four images are corrupted by severe intensity inhomogeneity. The proposed method can provide satisfactory segmentation results for all cases. Therefore, the proposed method can segment images with severe intensity inhomogeneity.

With the inhomogeneous image model in (1), two types of synthetic images are generated. Each type of image uses the same homogenous image with 15 different degrees of intensity inhomogeneity. Fig. 3 shows the segmentation results on some of the two types of synthetic images by the proposed method. Fig. 4 shows the scale interval Δs between adjacent layers and the number of layers m in the proposed method. The degree of

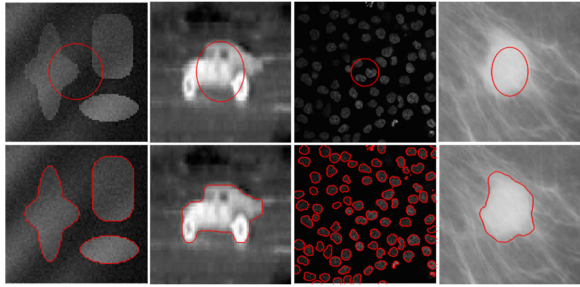


Fig. 2 Segmentation results by the proposed method on four images with severe intensity inhomogeneity. The first row is the original images with red initial contours and the second row is the segmentation results

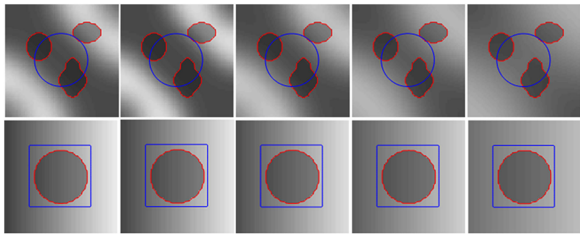


Fig. 3 Segmentation results of the proposed method on synthetic images with different degrees of intensity inhomogeneity. The blue lines are the initial contours and the red lines are the corresponding segmentation results

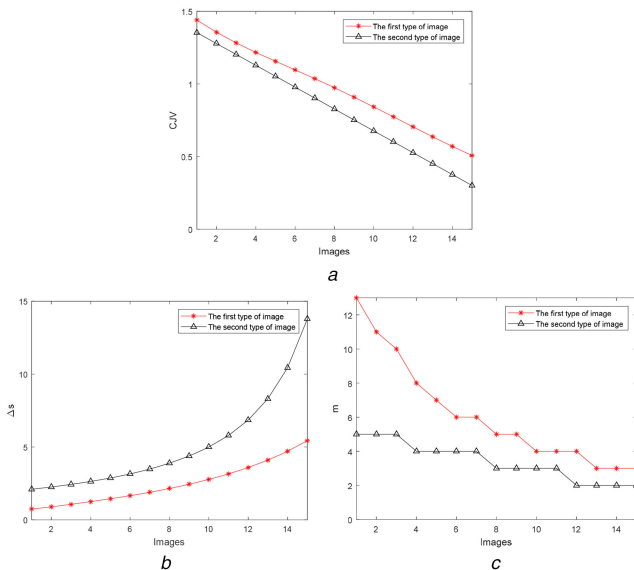


Fig. 4 Scale interval Δs between adjacent layers and the number of layers m of the proposed method on two types of synthetic images
(a)–(c) CJV values, the proposed Δs and m , respectively

intensity inhomogeneity decreases gradually for the two types of synthetic images, as shown in Fig. 4a. The results show that the method can obtain satisfactory segmentation results. As the degree of intensity inhomogeneity decreases, the scale interval between adjacent layers increases and the number of layers decreases. Therefore, the proposed method can adaptively determine the scale parameters according to the degree of the image intensity inhomogeneity.

4.1 Detailed analysis

4.1.1 Effectiveness of the adaptive scale operators: In this section, a single layer level set method based on bias correction is utilised to demonstrate the effectiveness of the adaptive scale operators. The order of the level set evolution and the bias field estimation of the LIC model is switched, called the order local intensity clustering (OLIC) model, to make the model robust to initial contour. The OLIC model is applied to the first type of

synthetic images applied in Fig. 4, as shown in Fig. 5. The intensity inhomogeneity of the images is gradually decreasing. μ is set to 0 in the experiments to remove the length item in the OLIC model. The initial contour is close to the real boundary of the object to reduce the impact of initial contour. As is seen from Fig. 5a, images with different degree of intensity inhomogeneity require different scale parameters. From Fig. 5b, it is clear that the global adaptive scale parameters with $\alpha = 12$ are close to the maximum feasible scale parameters, which is the maximum scale to segment the image correctly by the OLIC model for every image. For $\alpha = 2.3 - 11.5$, the global adaptive scale parameters can ensure that the OLIC model segments every image correctly, as shown in Fig. 5c. Considering the accuracy and efficiency α is set to 5.2 in the experiments. Therefore, the global adaptive scale operator is effective for the OLIC model to handle inhomogeneous images.

Fig. 6 shows the segmentation results of the LIC model with the global adaptive scale operator (LICG), the OLIC model with the global adaptive scale operator (OLICG) and the OLIC model with the local adaptive scale operator (OLICL) on five inhomogeneous images. μ is set to 0.001×255^2 , 0.0003×255^2 , 0.001×255^2 , and 0.001×255^2 for the second, third, fourth, and fifth image, respectively. For the first two images with slight intensity inhomogeneity, all of the three models can obtain satisfactory segmentation results. The OLICG and the OLICL model provides satisfactory segmentation results for the first four images. In particular, the OLICL model can obtain more accurate segmentation results than the OLICG model for images with weak boundaries, as shown in rows 2 and 5 of Fig. 6. From column 5 of Fig. 6, it is obvious that the region with large intensity variation has small scale parameters, especially in the object boundary region, and the region with small intensity variation has large scale parameters. Therefore, the proposed local adaptive scale operator is effective to segment inhomogeneous images. In order to analyse the robustness to the initial contour, the OLICG and OLICL models are applied to one synthetic inhomogeneous image with different initial contours, as shown in Fig. 7. It can be seen that the OLICG and OLICL models are sensitive to the initial contours.

4.1.2 Effectiveness of the adaptive multilayer structure: Since the multilayer structure of the proposed method is similar to the DM model, the DM model is utilised to illustrate the effectiveness of the proposed scale interval Δs and the number of layers m . The DM model with the proposed Δs or m is applied to the first type of images applied in Fig. 4, as shown in Fig. 8. The DM model with proposed Δs or m can obtain better segmentation results than the DM model, and the DM model with adaptive multilayer structure (DMAM) constructed by the proposed Δs and m achieves the best performance, as shown in Fig. 8a. In this experiment, the number of the iterations of the model with an incorrect segmentation result is set to the maximum number of iterations. DM model with the proposed Δs has slightly weaker performance than the DMAM model, as shown in Figs. 8b and c. However, the iterations and the computing time of the DM model with the proposed Δs is significantly higher than the DMAM model on the last seven images with slight intensity inhomogeneity. For the first seven images with severe intensity inhomogeneity, the DM model with the proposed m needs more iterations compared with the DMAM model or fails to segment the images. The DMAM model has higher segmentation efficiency than the other three models. Therefore, the adaptive multilayer structure constructed by the proposed Δs and m are effective to segment inhomogeneous images.

The influence of the parameter β in $\Delta s = \beta\sigma_{b0}$ is discussed for the DMAM model. The DMAM model is applied to the first type of synthetic images applied in Fig. 4 with different β , as shown in Fig. 9. The DMAM model can achieve correct segmentation results for all cases. Meanwhile, the DMAM model can achieve the minimum mean of the number of the iterations when β is near 0.95, while smaller or larger β requires more iterations. Considering the efficiency β is set to 0.95 in the experiments.

Fig. 10 shows the segmentation results of the DM model, the DMAM model and the proposed AMLLS model with the initial

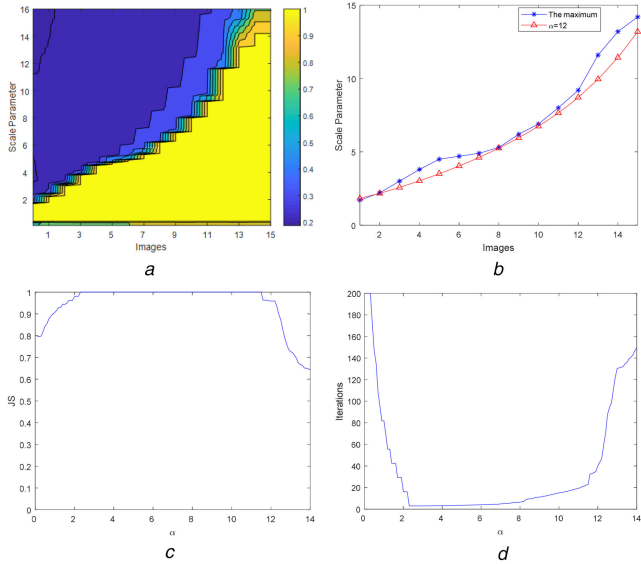


Fig. 5 Effectiveness of the global adaptive scale operator

(a) JS values of the OLIC model on different images with scale parameters varying from 0 to 16, (b) The estimated global adaptive scale parameters with $\alpha = 12$, (c), (d) The mean of the JS values and iterations by the OLIC model with α varying from 0 to 14, respectively

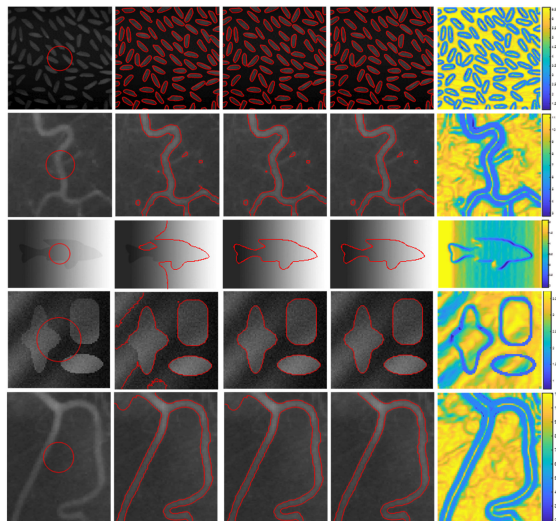


Fig. 6 Comparison of LICG, OLICG, and OLICL models. From the first to last column: the original images with red initial contours, the results of the LICG, OLICG, and OLICL models, and the local adaptive scale parameters

bias field (AMLLS_I) on two synthetic images and one medical image. μ is set to 0.002×255^2 for the second image in the experiments. The DM model obtains a satisfactory segmentation result on the third image with slight intensity inhomogeneity, but is not able to segment the first two images with severe intensity inhomogeneity. The DMAM model and the AMLLS_I model can obtain similar and satisfactory segmentation results for the three images with different intensity inhomogeneity. Meanwhile, the AMLLS_I model can obtain better segmentation results than the other two model especially for images with weak boundaries, as shown in rows 2 and 3 of Fig. 10. Therefore, the proposed adaptive multilayer structure is effective in segmenting images with intensity inhomogeneity.

4.1.3 Effectiveness of the hybrid bias field: To demonstrate the effectiveness of the hybrid bias field, the AMLLS_I model, the AMLLS model with the estimated bias field (AMLLS_E) and the proposed AMLLS model are applied to two images with severe intensity inhomogeneity, as shown in Fig. 11. μ is set to 0.0003×255^2 for the third image in the experiments. It can be

observed that the AMLLS_E model is sensitive to the initial contour, while the AMLLS_I is not. For the image with the large intensity overlap between object and background, the AMLLS_I model is not able to obtain the correct segmentation result, while the AMLLS_E model is able to do so, as shown in row 3 of Fig. 11. The AMLLS model can obtain satisfactory segmentation results for all cases, as shown in column 4 of Fig. 11. Therefore, the hybrid bias field can enhance the robustness of the proposed method.

4.2 Performance evaluation and method comparison

In this section, the proposed method is qualitatively analysed and compared with some segmentation methods.

4.2.1 Robustness to the initial contour: Fig. 12 shows the segmentation results of the proposed method on three synthetic inhomogeneous images with six different initial contours. All three images have severe intensity inhomogeneity, and the proposed method obtains satisfactory segmentation results for different initial contours. Therefore, the proposed method can deal with images with severe intensity inhomogeneity and is robust to initial contour.

To quantitatively analyse the performance on different initial contours, the proposed AMLLS method is applied to one medical image with 15 different initial contours, as shown in Fig. 13. μ is set to 0.0003×255^2 in the experiments. The proposed method obtains satisfactory segmentation results for different initial contours on the image. The proposed AMLLS method is also compared with the MSF, LICD, LSACM, DM, and LINC models. The corresponding JS values of the segmentation results are shown in Fig. 14. It clearly demonstrates that the proposed method achieves very high and stable segmentation accuracy for different initial contours. Therefore, the proposed method is robust to initial contour.

4.2.2 Robustness to the degree of intensity inhomogeneity: To demonstrate the performance of the proposed method in terms of the robustness to the degree intensity inhomogeneity, the proposed AMLLS method is quantitatively compared with the LIC, LSACM, ASACM, FLSAS, MSF, and DM models, as shown in Fig. 15. These seven models are applied to the two types of synthetic images with different intensity inhomogeneity applied in Fig. 4. The degree of intensity inhomogeneity decreases gradually for the two types of synthetic images. It can be seen that the LIC, LSACM, MSF, and DM models with fixed scale parameters can segment weakly inhomogeneous images, but cannot obtain correct segmentation results for images with severe inhomogeneity. The ASACM and FLSAS models using adaptive scale parameters obtain better segmentation results than the previous four methods. The FLSAS model is better than the ASACM method. The proposed AMLLS model can obtain accurate segmentation results for all cases. Therefore, the proposed method is robust to the degree intensity inhomogeneity.

4.2.3 Accuracy and efficiency comparison: The proposed AMLLS model is compared with eight representative level set methods including the LBF, LIC, MSF, LICD, LSACM, DM, LINC, and FLSAS models on three synthetic images, one infrared image and four medical images with intensity inhomogeneity, as shown in Fig. 16. The eight models select optimal parameters in the experiments. For the AMLLS model, μ is set to 0.001×255^2 , 0.0003×255^2 , 0.0001×255^2 , 0.02×255^2 , 0.001×255^2 , 0.0003×255^2 , 0.00255×255^2 , and 0.0026×255^2 for the images in the experiments, respectively. Most of the models can obtain satisfactory segmentation results on images with slight intensity inhomogeneity, as shown in columns 1, 5, 6, and 7 of Fig. 16. For images with severe intensity inhomogeneity, most of the models cannot obtain satisfactory segmentation results, as shown in columns 2, 3, 4, and 8 of Fig. 16. The proposed AMLLS model can obtain satisfactory segmentation results for all cases. The JS value

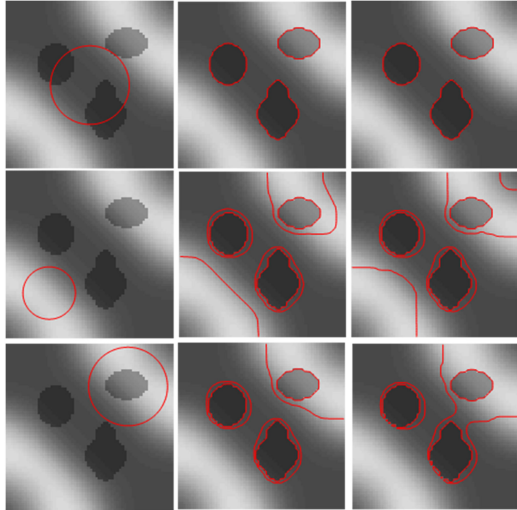
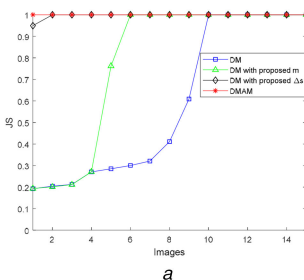
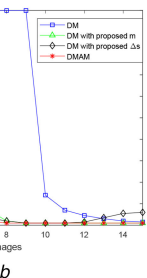


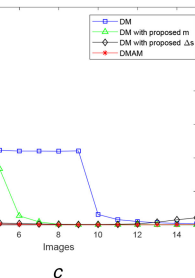
Fig. 7 Segmentation results of the OLICG and OLICL models on one inhomogeneous image with different initial contours. From the first to last column: image with different initial contours, results of the OLICG and OLICL models



a



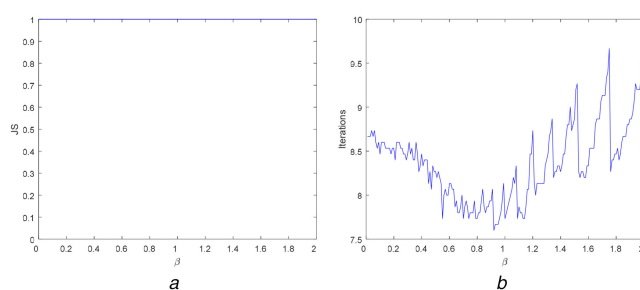
b



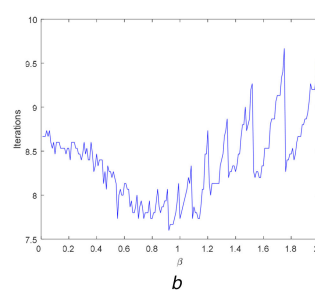
c

Fig. 8 Effectiveness of the proposed Δs and m for the DM model on 15 synthetic images with different degrees of intensity inhomogeneity

(a) JS values of the DM model, the DM model with proposed m , the DM model with proposed Δs and the DMAM model, respectively, (b) Iterations of the four models, (c) Computing time of the four models



a



b

Fig. 9 Influence of the parameter β for the DMAM model on the images with different degrees of intensity inhomogeneity

(a) The mean of JS values, (b) The mean of iterations

is utilised to quantitatively analyse the segmentation accuracy of these models, as shown in Table 1. The AMLLS model has the highest segmentation accuracy for most of the images. From the mean of the JS values for all images, it can be observed that the LBF achieves the worst segmentation results and the LIC model

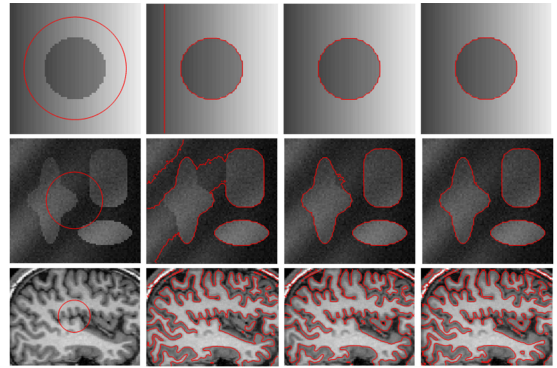


Fig. 10 Segmentation results of the DM, DMAM, and AMLLS_I models on two synthetic images and one medical image. From the first to last column: the original image, the results of the DM, DMAM, and AMLLS_I models

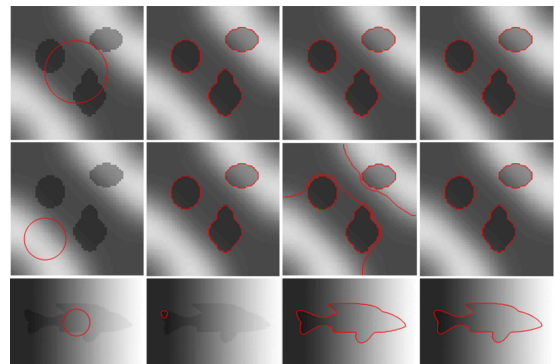


Fig. 11 Experimental results of the AMLLS_I, AMLLS_E, and AMLLS models. From the first to last column: the original image, the results of the AMLLS_I, AMLLS_E, and AMLLS models

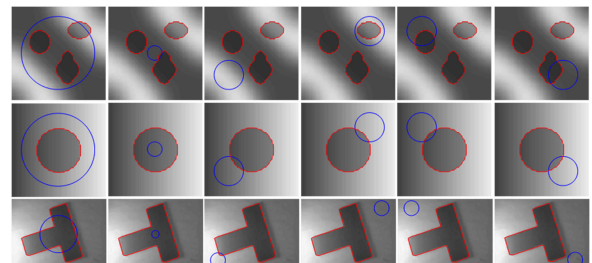


Fig. 12 Performances of the proposed method with different initial contours on three images with severe intensity inhomogeneity. The blue lines are the initial contours and the corresponding segmentation results are the red lines

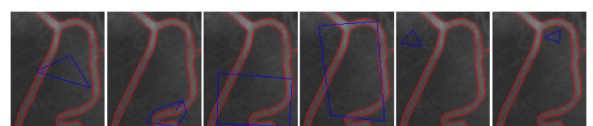


Fig. 13 Performances of the proposed method with different initial contours on one medical image with intensity inhomogeneity. The blue lines are the initial contours and the corresponding segmentation results are the red lines

follows. The MSF model, the LSACM model, the DM model, and the LINC model can achieve similar segmentation precision. The FLSAS model obtains the suboptimal segmentation results. The AMLLS model achieves the optimal segmentation results and significantly outperforms other models. These results demonstrate the superiority of the AMLLS model in terms of accuracy in segmenting inhomogeneous images. The corresponding computing time by the nine models for the images are shown in Table 2. The FLSAS model needs the least computing time for most images and the MSF model follows, which is because that the MSF model adopts MSF to estimate the bias field in advance. The AMLLS and

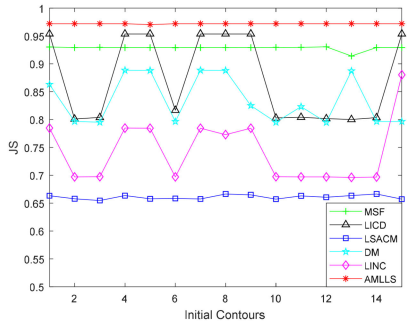


Fig. 14 JS values of the MSF, LICD, LSACM, DM, LINC, and AMLLS models on the image applied in Fig. 13 with different initial contours

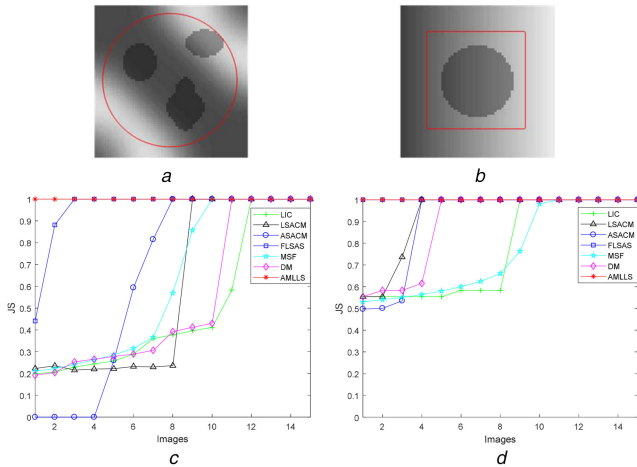


Fig. 15 Comparison of the LIC, LSACM, ASACM, FLSAS, MSF, DM, and AMLLS models on two types of images with different degrees of intensity inhomogeneity

(a), (b) The first image of each type of images, (c), (d) JS values of the seven models on the two types of images

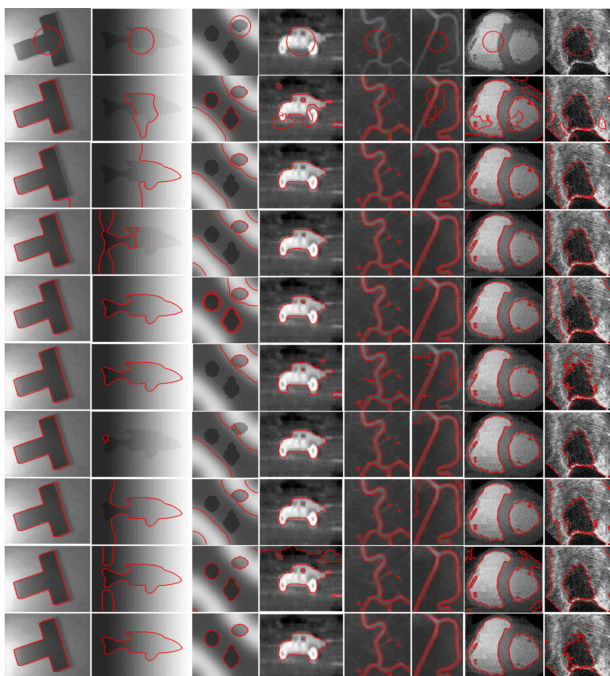


Fig. 16 Comparison of the proposed AMLLS method with eight representative models on eight inhomogeneous images. From the first to last row: the original image with initial contours, the results of the LBF, LIC, MSF, LICD, LSACM, DM, LINC, FLSAS, and AMLLS models

DM model spend more time than the other methods based on K -means clustering, which is because the two models have multilayer

structure. In addition, the AMLLS model converges faster than the DM model.

The proposed AMLLS method is also applied to the left ventricle magnetic resonance (LVMR) data set (the data is downloaded from [39]) and compared with some state-of-the-art segmentation methods such as: Otsu [40], Fuzzy c -means (FCM) [41], threshold selection by maximum entropy (MET) [42], continuous max-flow and min-cut approaches (CMF-C) [43], local Fuzzy thresholding methodology [44], slope difference distribution (SDD)-based threshold selection [45], CV [9], and distance-regularised level set (DRLS) [5]. The quantitative results are shown in Table 3. The average perpendicular distances (APD) and the Dice metric (DICE) [46] are utilised for the evaluation of the performance. SDD method obtains the best segmentation results. The AMLLS and MET methods are only slightly worse than the SDD method, but better than other methods. The level set-based methods are slower than the other methods. The proposed method is faster than the DRLS model and similar to the CV model.

4.3 Multi-phase segmentation

In the following experiments, the multi-phase level set formulation of the proposed model is applied to segment the multi-phase brain magnetic resonance images (MRI). It is an important task to segment the brain MR images into white matter (WM), grey matter (GM), cerebrospinal fluid (CSF) in medical image analysis. The proposed AMLLS model is compared with the LIC, HRIF, and FLSAS models on simulated MRI volumes (the data can be downloaded from [47]) for the normal brain with 40% intensity inhomogeneity. α is set to ten in the multiphase segmentation experiments.

Fig. 17 shows the segmentation results of the LIC, HRIF, FLSAS, and AMLLS models on four inhomogeneous brain MRI. It can be seen that the HRIF model cannot obtain accurate segmentation results in the regions with weak boundaries. The other three models achieve satisfactory segmentation results for all cases. The JS values for WM, GM, and CSF by the LIC, HRIF, FLSAS, and AMLLS models on the four brain MRI are shown in Table 4. It can be seen that the proposed AMLLS method has higher JS values than the other three models, especially for GM and CSF segmentation. Therefore, the proposed AMLLS models are effective to segment multi-phase inhomogeneous images.

5 Conclusions

In this paper, an AMLLS method is proposed to segment images with severe intensity inhomogeneity. Local variance is utilised to measure the local image inhomogeneity. An improved global adaptive scale operator and a local adaptive scale operator for clustering kernel function are designed based on the local variance. Then, an AMLLS structure is constructed with the two designed scale operators. The number of layers and the scale of each layer in the multilayer structure is adaptively determined based on the degree of intensity inhomogeneity, which not only provides appropriate candidate scales in each pixel, but also allows the model to detect global contrast information. With the DM method, image segmentation and bias correction can be achieved simultaneously. In addition, a hybrid bias field initialisation procedure is proposed based on the CJV to enhance the robustness of the proposed method. The experimental results on synthetic and real images show that the proposed method can segment inhomogeneous images accurately, and it is robust to initial contour.

6 Acknowledgments

This work was supported by the National Natural Science Foundation of China under grant No. 61501357 and the Basic science research project of Shaanxi Province under grant No. 2016JQ6080.

Table 1 Comparison of JS values for the nine models on images in Fig. 16

Methods	LBF	LIC	MSF	LICD	LSACM	DM	LINC	FLSAS	AMLLS
image 1	0.9909	0.4361	0.9777	0.9874	0.9496	0.9867	0.9562	0.9770	0.9912
image 2	0.3780	0.3105	0.2402	0.9976	0.9869	0.0262	0.4860	0.7434	0.9941
image 3	0.0562	0.2135	0.2098	0.1599	0.1595	0.1908	0.1993	0.9549	1.0000
image 4	0.5549	0.8941	0.8902	0.8872	0.8180	0.9514	0.8907	0.5330	0.9932
image 5	0.6673	0.9641	0.9439	0.9630	0.7238	0.9427	0.8971	0.9161	0.9840
image 6	0.4974	0.8120	0.9305	0.8011	0.4031	0.7949	0.6985	0.9324	0.9721
image 7	0.6960	0.9999	0.9380	0.9898	0.9370	0.9372	0.9722	0.8236	0.9324
image 8	0.6072	0.6950	0.7593	0.5484	0.7967	0.9999	0.6655	0.7319	0.8591
mean	0.5560	0.6657	0.7362	0.7918	0.7218	0.7287	0.7207	0.8265	0.9658

Table 2 Computing time(s) for the nine models on images in Fig. 16

Methods	LBF	LIC	MSF	LICD	LSACM	DM	LINC	FLSAS	AMLLS
image 1	7.3022	11.2564	1.0358	4.7492	1.3757	13.4826	11.9466	0.1607	6.1641
image 2	10.0946	13.8559	0.7201	6.1959	9.5576	31.4518	12.3697	0.1036	17.8007
image 3	5.4706	3.9977	0.3109	0.8413	0.8470	11.3980	1.3548	0.0172	3.1408
image 4	7.9840	7.1697	0.7052	3.5768	2.6105	99.4779	8.1663	0.2387	4.1615
image 5	7.9490	9.1507	1.4993	6.0296	2.8416	28.9356	1.9709	0.1119	15.0781
image 6	8.5673	10.6381	1.4603	7.6637	8.5481	25.3225	5.1503	0.1386	40.8311
image 7	22.9782	12.6112	1.0160	10.9668	56.9010	27.0209	6.3338	0.3386	9.7014
image 8	6.8338	9.0936	0.6091	3.9724	7.0098	52.8290	3.4750	0.1507	11.1821
mean	9.6475	9.7217	0.9196	5.4995	11.2114	36.2398	6.3459	0.1575	13.5075

Table 3 APD, DICE, and computing time (s) for AMLLS and eight state-of-the-art segmentation methods on LVMR data set

	Otsu	FCM	MET	CMF-C	LFM	SDD	CV	DRLS	AMLLS
mean (APD)	2.5019	4.0116	2.2547	3.9578	2.7622	2.1128	3.7840	6.0538	2.2541
mean (DICE)	0.8927	0.8116	0.9060	0.8451	0.8822	0.9118	0.8466	0.7783	0.9041
mean (time)	0.0027	0.1410	0.0096	0.0194	0.0179	0.0326	0.9995	4.0904	1.0128

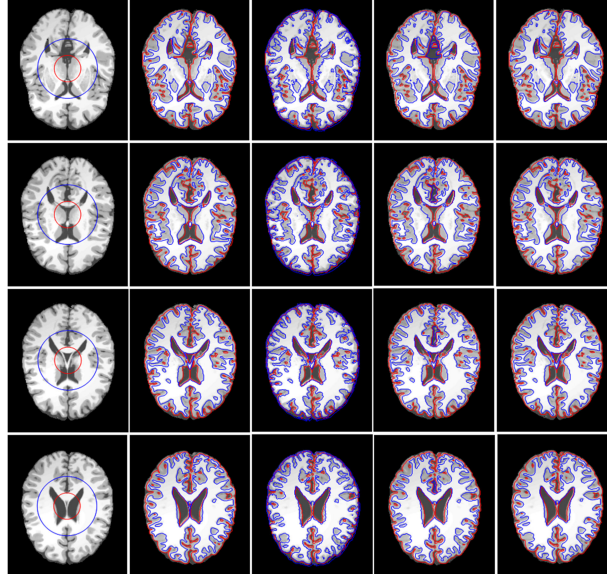
**Fig. 17** Comparisons of the proposed AMLLS method with the LIC, HRIF, and FLSAS models on four inhomogeneous brain MRI. From the first to last column: the original images with initial contours of two-level set functions: ϕ_1 (the red lines) and ϕ_2 (the blue lines), the segmentation results of the LIC, HRIF, FLSAS, and AMLLS models

Table 4 JS values for WM, GM, and CSF by the LIC, HRF, FLSAS, and AMLLS models on images in Fig. 17

Methods	LIC			HRIF			FLSAS			AMLLS		
	CSF	GM	WM									
image 1	0.9375	0.9204	0.9424	0.8194	0.6126	0.7366	0.9292	0.9125	0.9370	0.9540	0.9277	0.9441
image 2	0.9281	0.9254	0.9481	0.8073	0.6116	0.7266	0.9219	0.9207	0.9442	0.9465	0.9335	0.9492
image 3	0.9344	0.9352	0.9683	0.8237	0.6114	0.7798	0.9237	0.9279	0.9654	0.9520	0.9412	0.9673
image 4	0.9418	0.9306	0.9682	0.8332	0.6125	0.7976	0.9352	0.9285	0.9674	0.9581	0.9402	0.9693
mean	0.9355	0.9279	0.9568	0.8209	0.6120	0.7602	0.9275	0.9224	0.9535	0.9527	0.9357	0.9575

7 References

- [1] Li, C., Huang, R., Ding, Z., et al.: ‘A level set method for image segmentation in the presence of intensity inhomogeneities with application to MRI’, *IEEE Trans. Image Process.*, 2011, **20**, (7), pp. 2007–2016
- [2] Kass, M., Witkin, A., Terzopoulos, D.: ‘Snakes: active contour models’, *Int. J. Comput. Vis.*, 1988, **1**, (4), pp. 321–331
- [3] Osher, S., Sethian, J.A.: ‘Fronts propagating with curvature-dependent speed: algorithms based on Hamilton-Jacobi formulations’, *J. Comput. Phys.*, 1988, **79**, (1), pp. 12–49
- [4] Caselles, V., Kimmel, R., Sapiro, G.: ‘Geodesic active contours’, *Int. J. Comput. Vis.*, 1997, **22**, (1), pp. 61–79
- [5] Li, C., Xu, C., Gui, C., et al.: ‘Distance regularized level set evolution and its application to image segmentation’, *IEEE Trans. Image Process.*, 2010, **19**, (12), pp. 3243–3254
- [6] Ali, H., Badshah, N., Chen, K., et al.: ‘A variational model with hybrid images data fitting energies for segmentation of images with intensity inhomogeneity’, *Pattern Recognit.*, 2016, **51**, pp. 27–42
- [7] Liu, C., Liu, W., Xing, W.: ‘An improved edge-based level set method combining local regional fitting information for noisy image segmentation’, *Signal Process.*, 2017, **130**, pp. 12–21
- [8] Wang, L., Chen, G., Shi, D., et al.: ‘Active contours driven by edge entropy fitting energy for image segmentation’, *Signal Process.*, 2018, **149**, pp. 27–35
- [9] Chan, T.F., Vese, L.A.: ‘Active contours without edges’, *IEEE Trans. Image Process.*, 2001, **10**, (2), pp. 266–277
- [10] Liu, Y., He, C., Wu, Y., et al.: ‘The L_0 -regularized discrete variational level set method for image segmentation’, *Image Vis. Comput.*, 2018, **75**, pp. 32–43
- [11] Wu, Y., He, C.: ‘A convex variational level set model for image segmentation’, *Signal Process.*, 2015, **106**, pp. 123–133
- [12] Zhang, K., Zhang, L., Song, H., et al.: ‘Active contours with selective local or global segmentation: new formulation and level set method’, *Image Vis. Comput.*, 2010, **28**, (4), pp. 668–676
- [13] Dong, F., Chen, Z., Wang, J.: ‘A new level set method for inhomogeneous image segmentation’, *Image Vis. Comput.*, 2013, **31**, (10), pp. 809–822
- [14] Wang, X.-F., Zou, L., Xu, L.-X., et al.: ‘Hybrid level set method based on image diffusion’, *Neurocomputing*, 2017, **228**, pp. 53–64
- [15] Mumford, D., Shah, J.: ‘Optimal approximations by piecewise smooth functions and associated variational problems’, *Commun. Pure Appl. Math.*, 1989, **42**, (5), pp. 577–685
- [16] Li, C., Kao, C., Gore, J.C., et al.: ‘Implicit active contours driven by local binary fitting energy’, 2007 IEEE Conf. on Computer Vision and Pattern Recognition, Minneapolis, USA, 2007, pp. 1–7
- [17] Li, C., Kao, C.-Y., Gore, J.C., et al.: ‘Minimization of region-scalable fitting energy for image segmentation’, *IEEE Trans. Image Process.*, 2008, **17**, (10), pp. 1940–1949
- [18] Wang, X.-F., Huang, D.-S., Xu, H.: ‘An efficient local Chan-Vese model for image segmentation’, *Pattern Recognit.*, 2010, **43**, (3), pp. 603–618
- [19] Zhang, K., Song, H., Zhang, L.: ‘Active contours driven by local image fitting energy’, *Pattern Recognit.*, 2010, **43**, (4), pp. 1199–1206
- [20] Ji, Z., Xia, Y., Sun, Q., et al.: ‘Active contours driven by local likelihood image fitting energy for image segmentation’, *Inf. Sci.*, 2015, **301**, pp. 285–304
- [21] Wang, L., Chang, Y., Wang, H., et al.: ‘An active contour model based on local fitted images for image segmentation’, *Inf. Sci.*, 2017, **418–419**, pp. 61–73
- [22] Chen, Y., Yue, X., Xu, R.Y.D., et al.: ‘Region scalable active contour model with global constraint’, *Knowl.-Based Syst.*, 2017, **120**, pp. 57–73
- [23] Min, H., Lu, J.T., Jia, W., et al.: ‘An effective local regional model based on salient fitting for image segmentation’, *Neurocomputing*, 2018, **311**, pp. 245–259
- [24] Vovk, U., Pernus, F., Likar, B.: ‘A review of methods for correction of intensity inhomogeneity in MRI’, *IEEE Trans. Med. Imaging*, 2007, **26**, (3), pp. 405–421
- [25] Li, C., Gore, J.C., Davatzikos, C.: ‘Multiplicative intrinsic component optimization (MICO) for MRI bias field estimation and tissue segmentation’, *Magn. Reson. Imaging*, 2014, **32**, (7), pp. 913–923
- [26] Feng, C., Zhao, D., Huang, M.: ‘Image segmentation and bias correction using local inhomogeneous iNTensity clustering (LINC): a region-based level set method’, *Neurocomputing*, 2017, **219**, pp. 107–129
- [27] Zhan, T., Zhang, J., Xiao, L., et al.: ‘An improved variational level set method for MR image segmentation and bias field correction’, *Magn. Reson. Imaging*, 2013, **31**, (3), pp. 439–447
- [28] Zhang, K., Zhang, L., Lam, K.-M., et al.: ‘A level set approach to image segmentation with intensity inhomogeneity’, *IEEE Trans. Cybern.*, 2016, **46**, (2), pp. 546–557
- [29] Zhang, K., Liu, Q., Song, H., et al.: ‘A variational approach to simultaneous image segmentation and bias correction’, *IEEE Trans. Cybern.*, 2015, **45**, (8), pp. 1426–1437
- [30] Huang, C., Zeng, L.: ‘An active contour model for the segmentation of images with intensity inhomogeneities and bias field estimation’, *PLoS ONE*, 2015, **10**, (4), pp. 1–24
- [31] Wang, L., Zhu, J., Sheng, M., et al.: ‘Simultaneous segmentation and bias field estimation using local fitted images’, *Pattern Recognit.*, 2018, **74**, pp. 145–155
- [32] Piovano, J., Papadopoulou, T.: ‘Local statistic based region segmentation with automatic scale selection’, European Conf. on Computer Vision (ECCV 2008), Marseille, France, 2008, pp. 486–499
- [33] Cai, Q., Liu, H., Zhou, S., et al.: ‘An adaptive-scale active contour model for inhomogeneous image segmentation and bias field estimation’, *Pattern Recognit.*, 2018, **82**, pp. 79–93
- [34] Huang, G., Ji, H., Zhan, W.: ‘A fast level set method for inhomogeneous image segmentation with adaptive scale parameter’, *Magn. Reson. Imaging*, 2018, **52**, pp. 33–45
- [35] Sui, H.G., Xu, C., Liu, J.Y., et al.: ‘A novel multi-scale level set method for SAR image segmentation based on a statistical model’, *Int. J. Remote Sens.*, 2012, **33**, (17), pp. 5600–5614
- [36] Wang, X.-F., Min, H., Zhang, Y.-G.: ‘Multi-scale local region based level set method for image segmentation in the presence of intensity inhomogeneity’, *Neurocomputing*, 2015, **151**, (3), pp. 1086–1098
- [37] Min, H., Wang, X.-F., Huang, D.-S., et al.: ‘A novel dual minimization based level set method for image segmentation’, *Neurocomputing*, 2016, **214**, pp. 910–926
- [38] Zhang, K., Zhang, L., Song, H., et al.: ‘Reinitialization-free level set evolution via reaction diffusion’, *IEEE Trans. Image Process.*, 2013, **22**, (1), pp. 258–271
- [39] ‘Image segmentation methods Comparison with MRI’, Available at: <https://www.mathworks.com/matlabcentral/fileexchange/62574-image-segmentation-methods-comparison-with-mri>, accessed 25 April 2019
- [40] Otsu, N.: ‘A threshold selection method from gray-level histograms’, *IEEE Trans. Syst. Man Cybern.*, 1979, **9**, (1), pp. 62–66
- [41] Bezdek, J.C., Ehrlich, R., Full, W.: ‘FCM: the Fuzzy c-means clustering algorithm’, *Comput. Geosci.*, 1984, **10**, pp. 191–203
- [42] Sezgin, M., Sankur, B.: ‘Survey over image thresholding techniques and quantitative performance evaluation’, *J. Electron. Imaging*, 2004, **13**, (1), pp. 146–168
- [43] Yuan, J., Bae, E., Tai, X.C.: ‘A study on continuous max-flow and min-cut approaches’, 2010 IEEE Computer Society Conf. on Computer Vision and Pattern Recognition, San Francisco, USA, 2010, pp. 2217–2224
- [44] Aja-Fernandez, S., Curiale, A.H., Vegas-Sanchez-Ferrero, G.: ‘A local Fuzzy thresholding methodology for multiregion image segmentation’, *Knowl.-Based Syst.*, 2015, **83**, pp. 1–12
- [45] Wang, Z.Z.: ‘A new approach for segmentation and quantification of cells or nanoparticles’, *IEEE Trans. Ind. Inf.*, 2016, **12**, (3), pp. 962–971
- [46] Wang, Z.Z.: ‘Segmentation of the left ventricle in short-axis sequences by combining deformation flow and optical flow’, *IET Image Process.*, 2017, **11**, (4), pp. 237–244
- [47] ‘BrainWeb: Simulated Brain Database’, available at: <http://brainweb.bic.mni.mcgill.ca/brainweb>, accessed 12 March 2019